JACS
JOURNAL OF THE AMERICAN CHEMICAL SOCIETY
pubs.acs.org/JACS
Article

Machine Learning Guided Synthesis of Multinary Chevrel Phase Chalcogenides

Nicholas R. Singstock, Jessica C. Ortiz-Rodríguez, Joseph T. Perryman, Christopher Sutton, Jesús M. Velázquez,* and Charles B. Musgrave*

Cite This: J. Am. Chem. Soc. 2021, 143, 9113–9122
Read Online
ACCESS | Metrics & More | Article Recommendations | Supporting Information

ABSTRACT: The Chevrel phase (CP) is a class of molybdenum chalcogenides that exhibit compelling properties for next-generation battery materials, electrocatalysts, and other energy applications. Despite their promise, CPs are underexplored, with only ∼100 compounds synthesized to date due to the challenge of identifying synthesizable phases. We present an interpretable machine-learned descriptor (H_δ) that rapidly and accurately estimates decomposition enthalpy (ΔH_d) to assess CP stability. To develop H_δ, we first used density functional theory to compute ΔH_d for 438 CP compositions. We then generated >560 000 descriptors with the new machine learning method SIFT, which provides an easy-to-use approach for developing accurate and interpretable chemical models. From a set of >200 000 compositions, we identified 48 501 CPs that H_δ predicts are synthesizable based on the criterion that ΔH_d < 65 meV/atom, which was obtained as a statistical boundary from 67 experimentally synthesized CPs. The set of candidate CPs includes 2307 CP tellurides, an underexplored CP subset with a predicted preference for channel site occupation by cation intercalants that is rare among CPs. We successfully synthesized five of five novel CP tellurides attempted from this set and confirmed their preference for channel site occupation. Our joint computational and experimental approach for developing and validating screening tools that enable the rapid identification of synthesizable materials within a sparse class is likely transferable to other materials families to accelerate their discovery.

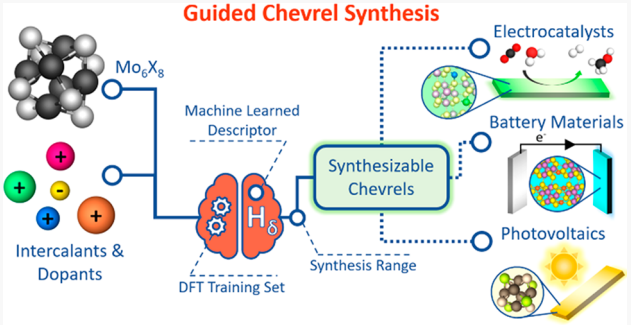

INTRODUCTION

Chevrel phases (CPs) are pseudomolecular solid molybdenum chalcogenides that have shown promise for a variety of applications. Although first explored in the 1970s as high-temperature superconductors,[1,2] a renewed interest in these materials was catalyzed by recent demonstrations of their potential as state-of-the-art monovalent and multivalent battery electrodes,[3−9] artificial solid-electrolyte interphases (SEI),[10,11] photovoltaics,[12] and electrocatalysts for hydrogen evolution,[13−15] oxygen reduction,[16] and CO_2 reduction.[17,18] The breadth of CP applications arises from their highly tunable electronic and thermodynamic properties (e.g., band gap,[12,19] band edge positions,[13,20] storage capacity,[21] ionic transport[22]) enabled by varying their composition (Figure 1a). Many thousands of multinary CP compositions are possible and are described by the general formula $M_yMo_6X_8$ ($0 \le y \le 4$), where M is an alkali, alkaline-earth metal, transition metal (TM), post-TM, lanthanide, or combinations thereof, and X is a chalcogen (S, Se, Te) or combination of chalcogens.

Despite their broad chemical space and favorable properties for multiple energy applications, the CP family is significantly underexplored, with only ∼100 synthesized compositions.[2] This is particularly evident for the CP tellurides, where only five multinary compositions have yet been synthesized.[23,24] Unfortunately, synthesizable CP compositions are not easily predicted because cation intercalation gives rise to competing effects on their stability.[25] As a result, determining the synthesizability of CP compositions generally requires computationally demanding *ab initio* calculations or experimental characterization. This poses a major obstacle to the discovery of new CPs. We propose that a rapid and accurate method to predict CP stability would greatly accelerate the discovery of new phases within this auspicious class of materials.

Machine learning (ML) has been used to accurately estimate density functional theory (DFT) formation enthalpies (ΔH_f) of materials.[26−29] However, decomposition enthalpies (ΔH_d) provide a more relevant metric for determining stability, where ΔH_d indicates the energy of a material relative to the convex

Received: March 18, 2021
Published: June 10, 2021

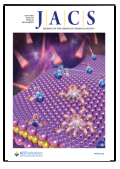

https://doi.org/10.1021/jacs.1c02971
J. Am. Chem. Soc. 2021, 143, 9113−9122

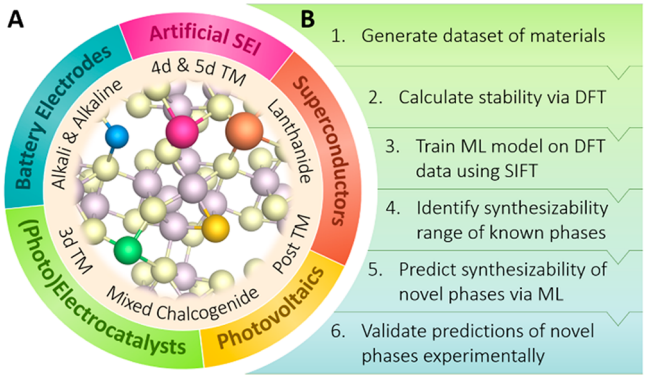

Figure 1. Expanding Chevrel phase materials. (A) The Mo_6X_8 CP framework can accept a broad range of intercalant elements to enable the tuning of many material properties of interest for advanced energy applications. (B) Computational and experimental approach used to discover synthesizable phases in the underexplored CP materials space. This approach is likely transferable to other material classes to accelerate their discovery.

hull (i.e., the minimum energy of all competing phases at the same elemental composition, see Experimental Section).[30] $\Delta H_d \leq 0$ indicates a stable material, whereas $\Delta H_d > 0$ indicates that a material is metastable or unstable. Herein, we report an accurate and interpretable ML descriptor, H_δ, for ΔH_d that requires only the CP composition as its input, thereby enabling exceedingly fast and highly accurate predictions of CP stability. H_δ was generated using symbolic regression with intermediate feature trimming (SIFT), a newly developed ML method that generates accurate and interpretable ML models from a large primary feature set. We created the largest computational data set of CPs to train H_δ using SIFT. This data set contains 438 compositions computed with the accurate SCAN functional (see Experimental Section) and expands the number of tabulated *ab initio* CP structures and enthalpies in existing materials databases by an order of magnitude. We applied H_δ to a set of 205 548 CP compositions and applied data-driven boundaries for ΔH_d that bracket stable and persistently metastable materials to identify 27 132 compositions that H_δ predicts are synthesizable as CPs via conventional high-temperature methods and another 21 369 that may be synthesizable with medium-temperature intercalation. We verified the ability of H_δ to predict new CPs by synthesizing five of five CP tellurides attempted from this set, doubling the space of known CP tellurides. We also demonstrate the failed synthesis of a CP telluride that H_δ predicts lies beyond the synthesizable boundary. Our approach to identify synthesizable CPs via DFT and ML, and to verify these predictions experimentally, is highlighted in Figure 1b. Because our approach does not require any parameters specific to the CP structure, it can be broadly applied to other material classes to accelerate their discovery. As interest in the unique CP class continues to grow, we expect the rapid identification of synthesizable CP compositions enabled by H_δ to catalyze the discovery of new materials and to facilitate further development of CP design criteria that correlate composition and functionality for relevant applications.

RESULTS AND DISCUSSION

Data Set Generation and Analysis. We generated 438 CPs with the formula $M_yMo_6X_8$, where X = S, Se, or Te and y = 0, 1, or 2. M is one of 53 elements that act as an intercalant cation that can occupy three unique sites around the Mo_6X_8 cluster: site 1, site 1 off-center, and site 2 (see Figure 2). The

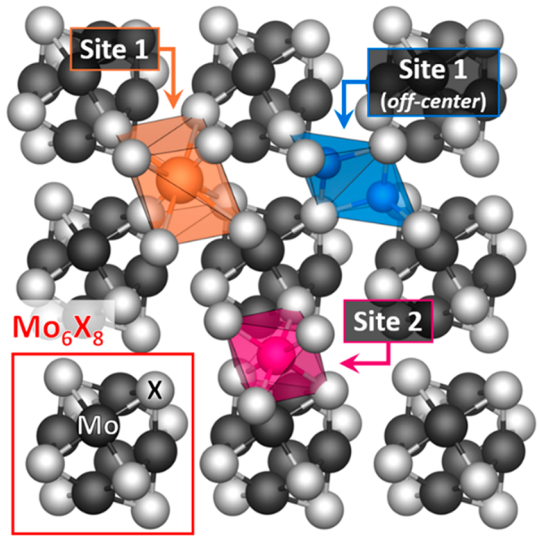

Figure 2. The CP structure. The CP crystal structure is composed of repeating Mo_6X_8 clusters (red) with cavities and channels between each cluster. This framework can host a variety of cation intercalants at three unique sites: site 1 is centered in the cavity between eight Mo_6X_8 clusters (orange), site 1 off-center includes other positions around the cavity (blue), and site 2 is a channel site that connects two cavities (magenta).

six Mo atoms form an octahedral cluster with 2 (4) Mo atoms with +2 (+3) charges, resulting in an average charge of +2.66 per Mo and an overall neutral charge for Mo_6X_8. The four Mo atoms with +3 charge can each be reduced to +2 upon cation intercalation, allowing for the total charge of the M cations to sum to +4 (e.g., a single intercalant with a +4 charge or four intercalants with a charge of +1 each).[31] Additionally, cation size regulates site preference and limits y.

For the 154 compositions in this set of 438 CPs with y = 1, we calculated ΔH_d for the three unique sites of the intercalant M. In order to show the relative differences in stability between these three sites and the trends in stability as the cation and chalcogenide are varied, we calculated the Boltzmann factor (i.e., the ratio of probabilities) between the ΔH_d of each site configuration and the lowest ΔH_d for the composition (see Experimental Section; note that entropy and zero-point energy were not included). These Boltzmann factors were normalized and plotted as stacked bars in Figure 3, where for each cation the areas indicate the degree of stability of each site. The most stable site configuration has the largest area, and the other sites have smaller areas that are proportional to the difference between their ΔH_d and the minimum ΔH_d. This analysis shows that large cations (e.g., alkali/alkaline, lanthanides, post-TMs) strongly prefer site 1 with hexahedral coordination (orange in Figure 2). In contrast, smaller cations (e.g., late 3d TMs) prefer site 1 off-center with tetrahedral coordination (blue in Figure 2). These observations are consistent with the literature.[2,31]

While site 2 is commonly occupied for $y > 1$,[32] occupation of site 2 at y = 1 has only been observed for the Mo_6Se_8 CPs intercalated with 3d TMs (Ti, Cr, Mn, Fe, Co, Ni).[33,34] However, our calculations predict that site 2 preference at y = 1 occurs among the CP sulfides with 4d and 5d TM

https://doi.org/10.1021/jacs.1c02971
J. Am. Chem. Soc. 2021, 143, 9113−9122

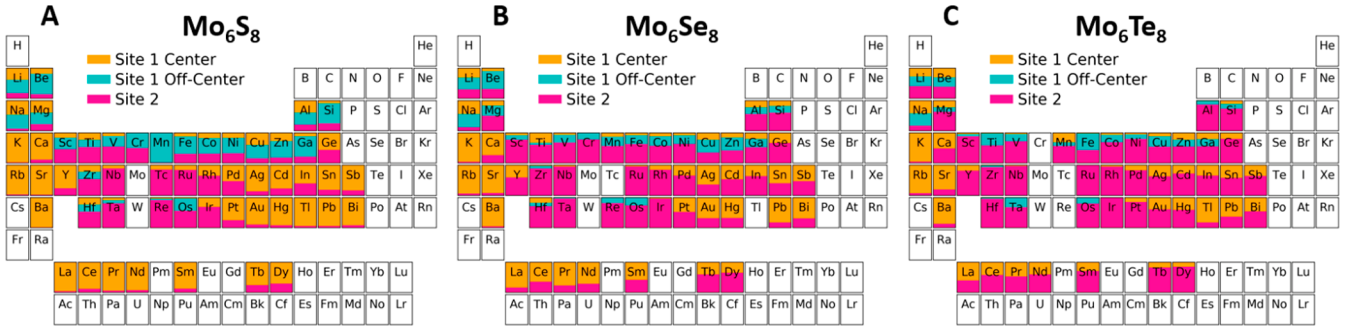

Figure 3. Intercalant site preference. Energetic preference for each site (see Figure 2) within the Mo_6X_8 framework as the identity of the intercalant M is varied in the Mo_6S_8 (A), Mo_6Se_8 (B), and Mo_6Te_8 (C) structures with $y = 1$. For each cation, the areas indicate the relative stability of each site, where a larger area indicates greater stability relative to competing polymorphs. Not all cations were studied for each chalcogenide due to the stochastic composition generation.

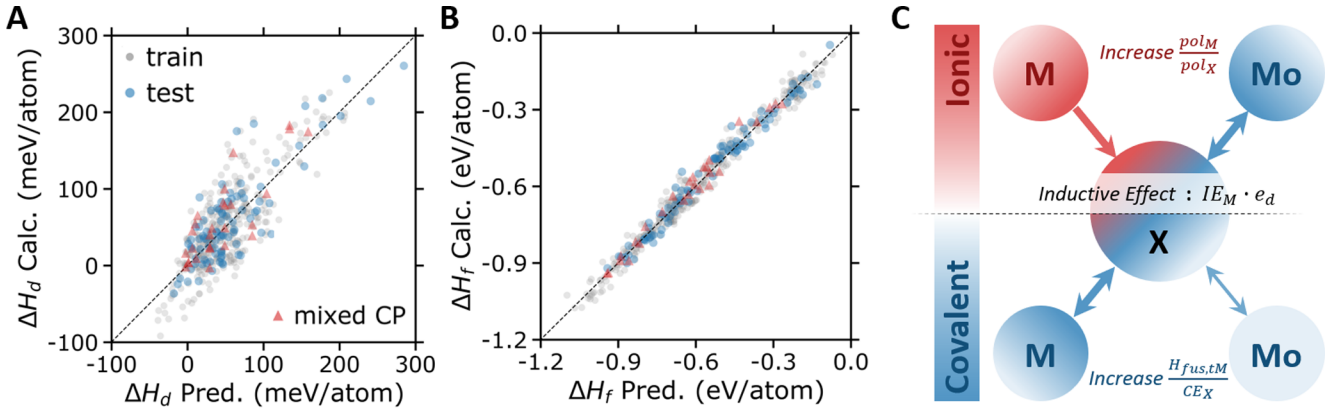

Figure 4. The machine-learned descriptor H_δ is accurate and interpretable. (A) H_δ reproduces CP ΔH_ds with mean absolute errors (MAEs) of 26 and 26 meV/atom and RMSEs of 33 and 33 meV/atom for the train (gray) and test (blue) sets, respectively. (B) Using ΔH_fs of competing phases, predicted ΔH_ds from H_δ can be converted to CP ΔH_fs without decreasing accuracy. Averaging chalcogenide features further enables H_δ to accurately predict ΔH_d of mixed-chalcogenide CPs (red triangles). (C) Multinary CP stability can be rationalized from H_δ as an ionic−covalent spectrum of M−X bonding. Greater ionicity of the M−X bond (red) increases the covalency of the Mo−X bond via the inductive effect, the magnitude of which is proportional to $IE_M e_d$; this increases overall CP stability.

intercalants (Figure 3a). Furthermore, a wealth of additional compounds exist with this site preference when X = Se or Te (Figure 3b and c). We expect these CPs to exhibit high cation mobility driven by exothermic migration into site 2 channels, which may have substantial implications for advanced battery materials (e.g., battery electrodes, artificial SEIs). The preference for occupying site 2 may also enable a new avenue for tuning catalytic reactivity in CPs due to a change in both the density of states and cation site occupancy that respectively contribute to ligand and ensemble effects that regulate adsorption kinetics on CP surfaces and nanoparticles.[17,18]

CPs with smaller cations can achieve $y > 1$.[31] Therefore, we also investigated 281 double-cation CP compositions (i.e., $M_2Mo_6X_8$ or $M^aM^bMo_6X_8$ for two different cations). These structures were initialized in two starting configurations: (a) with both cations occupying off-center positions neighboring site 1 (blue in Figure 2) and (b) with the larger cation in site 1 and the smaller cation in site 2 (orange and magenta, respectively, in Figure 2). These configurations constitute the variety of CP crystal structures observed in the literature.[2,31−33] In some cases, multiple initial configurations converged to the same final configuration; this was particularly common for $y = 1$ with large cations in site 1 and site 1 off-center.

In addition to analyzing the change in the stability of these sites upon variation of the intercalant, it is also important to investigate the impact of the site occupation on electronic structure. From our data set of 438 CPs, 42 are calculated to transition from metallic to semiconducting as the cation site changes (Table S1), and 83 are predicted to transition from nonmagnetic or antiferromagnetic to ferromagnetic as the cation site changes (Table S2). Properties such as the Fermi energy and unit cell volume vary with cation site occupation and may provide an approach to control cation site and thus conductivity and magnetic moment, which could enable advanced CP-based nanoelectronics.

Composition-Based Descriptor for Stability. We next trained an accurate and interpretable model using our database of calculated CP ΔH_ds and our new symbolic regression approach, which we call SIFT (see Experimental Section and Figure S1). The intermediate feature trimming step in SIFT enables the use of a large primary feature set that would not be computationally tractable using other symbolic regression approaches, such as the related SISSO (sure independence screening and sparsifying operator) algorithm,[35] where the size of the generated feature space greatly limits the number of primary features that can be examined.[36]

Starting from an initial set of 62 primary features, SIFT recursively applied a set of four mathematical operations over three iterations to develop increasingly complex combinations of features that describe ΔH_d (i.e., descriptors). Out of

https://doi.org/10.1021/jacs.1c02971
J. Am. Chem. Soc. 2021, 143, 9113−9122

>560 000 generated descriptors, H_δ (eq 1) yielded the lowest training set root mean squared error (RMSE) using an 80/20 train/test split of the 438 CP compositions, where only the minimum ΔH_d cation configuration for each CP was considered:

$$H_\delta = a\mathrm{IE_M}e_d\left(\frac{\mathrm{pol_M}}{\mathrm{pol_X}} - \left(\frac{H_{\mathrm{fus,tM}}}{\mathrm{CE_X}}\right)\right) + b \quad (1)$$

$\mathrm{IE_M}$ is the average first ionization energy of the cations (M) in eV/atom. e_d is the number of electrons donated from M to the Mo_6X_8 cluster, calculated from estimated oxidation states and bounded by $0 \le e_d \le 4$. $\mathrm{pol_M}$ and $\mathrm{pol_X}$ are the average electric dipole polarizabilities of M and X, respectively, in Å^3. $H_{\mathrm{fus,tM}}$ is the total enthalpy of fusion summed over all M(s) in eV/atom (i.e., $\sum_M y_M \Delta H_{\mathrm{fus,M}}$). $\mathrm{CE_X}$ is the average cohesive energy of X in eV/atom. a and b are fitted constants equal to −0.0380 (unitless) and 0.0297 (eV/atom), respectively. All features except e_d are tabulated, and elemental values for these are included in Table S3. H_δ yields predicted ΔH_d in eV/atom (i.e., $\Delta H_d = H_\delta$). Figure 4a shows the accuracy of H_δ on the training and testing sets, converted to meV/atom. CP ΔH_f values are calculated from the sum of the predicted ΔH_d (from H_δ) and the minimized ΔH_f of competing phases (see Experimental Section). Because only ΔH_d is predicted, ΔH_fs computed in this way have the same accuracy relative to DFT as the predicted ΔH_ds (Figure 4b).

Equation 1 can be decomposed into three combinations of features: $\mathrm{pol_M/pol_X}$, $H_{\mathrm{fus,tM}}/\mathrm{CE_X}$, and $\mathrm{IE_M}e_d$. The polarizability of the ions of a crystal greatly affects the localization of electrons and thus the overall ionic bonding.[37] Increasing the ratio of cation to chalcogen dipole polarizability $\mathrm{pol_M/pol_X}$ results in larger dipole moments and greater ionic bonding between M and X (i.e., increased ionicity, Figure 4c). This decreases H_δ and increases the stability of the multinary CPs, consistent with our recent results on 3d-TM intercalated sulfide CPs.[25] Conversely, increasing $H_{\mathrm{fus,tM}}/\mathrm{CE_X}$ increases H_δ and decreases stability. $H_{\mathrm{fus,tM}}$ and $\mathrm{CE_X}$ are measures of the total bond energy of the elemental solids M and X, respectively, which are composed of covalent or metallic M−M or X−X bonds. Increasing the total covalent/metallic bonding (i.e., covalency/metallicity) of M and decreasing the covalency (increasing metallicity) of X yields a more covalent M−X bond due to greater delocalization of electrons from X and increased electron sharing between M and X. Thus, the ratio $H_{\mathrm{fus,tM}}/\mathrm{CE_X}$ provides a gauge for the covalency of the M−X bond (Figure 4c). $\mathrm{pol_M/pol_X} - H_{\mathrm{fus,tM}}/\mathrm{CE_X}$, that is, the difference between M−X ionicity and covalency, indicates the degree of ionicity of M−X along the ionic−covalent bonding spectrum (Figure 4c). This is consistent with previous work that attributed the stability of intercalated CPs to competing shifts in ionic and covalent bonding that arise from the transfer of up to four electrons from M to the Mo_6X_8 cluster.[25,31]

The inductive effect has important consequences for the stability of multinary systems,[38] where greater covalent bonding between a cation and anion (i.e., M−X) reduces the covalent bonding between the same anion with another element (i.e., Mo−X).[39] Thus, the degree of ionicity of M−X regulates the inductive effect in CPs and the covalency of the Mo−X bond, which has been shown to drive overall covalent bonding in CPs.[25] A more ionic M−X bond yields a more covalent Mo−X bond and a more stable CP via greater ionicity and covalency, and *vice versa*. While $\mathrm{pol_M/pol_X} - H_{\mathrm{fus,tM}}/\mathrm{CE_X}$, regulates the position of M−X along the ionic−covalent spectrum, it does not determine the strength of these bonds. The term $\mathrm{IE_M}e_d$ of H_δ is approximately the ionization energy per electron multiplied by the number of donated electrons (i.e., overall ionization energy). Because the coefficient a is negative, this term quantifies the exothermicity of returning e_d electrons to M and therefore approximates the strength of the M−X bond. $\mathrm{IE_M}e_d$ is multiplied by $\mathrm{pol_M/pol_X} - H_{\mathrm{fus,tM}}/\mathrm{CE_X}$ to describe ΔH_d, and increasing $\mathrm{IE_M}e_d$ results in a greater contribution to the inductive effect in CPs (Figure 4c). When M−X is predominantly ionic ($\mathrm{pol_M/pol_X} > H_{\mathrm{fus,tM}}/\mathrm{CE_X}$), additional charge transfer to X arising from greater $\mathrm{IE_M}e_d$ increases the inductive effect and overall CP stability. Conversely, when M−X is more covalent in nature, increasing $\mathrm{IE_M}e_d$ increases M−X covalency and further destabilizes Mo−X bonding, reducing CP stability.

The performance of H_δ and SIFT relative to other ML models and a simple, physically motivated baseline model is analyzed in Section S1. This analysis indicates a trade-off between accuracy and simplicity, where H_δ provides superior accuracy over the baseline model (RMSE = 58.5 meV/atom) and over the other interpretable symbolic regression model (RMSE = 38.4 meV/atom). Although our goal was to generate a model that is both accurate and interpretable through low-dimensional linear regression, benchmarking against a high-dimensional nonlinear method provides a good lower bound on the error that can be obtained with our data set and features. The model based on kernel ridge regression (KRR) provides improved accuracy (RMSE = 17.7 meV/atom) relative to H_δ, but this comes at the cost of not being interpretable and the need for all 62 features to be input simultaneously. Therefore, the KRR model provides no insight regarding feature importance or the underlying chemical phenomena.

Metastability Range of Chevrel Phases. Sixty-seven of the CPs in our data set (Table S4) have been synthesized previously with a range of synthesis techniques.[19,22−25,32,34,40−56] These techniques can be classified as three general approaches, each used in a different temperature range: (a) direct high-temperature (T > 1000 C) synthesis from stoichiometric mixtures of the constituent elements and/or non-CP binaries (e.g., MoX_2); (b) medium-temperature ($T \approx$ 500 C) intercalation (MTI) of elemental M into Mo_6X_8; or (c) room-temperature intercalation of the dissolved cation M into Mo_6X_8. The large temperature differences between these different techniques indicate a wide range of stabilities of observed CPs.

Of the 67 previously synthesized CPs, DFT (H_δ) indicates that 34% (28%) are stable ($\Delta H_d \le 0$) and that the remaining 66% (72%) are unstable or metastable ($\Delta H_d > 0$). The 90th percentile of ΔH_d for these 67 CPs is 47 meV/atom (Figure S2), comparable to the 90th percentile of metastable sulfides and selenides observed in the literature.[57] Below this boundary, high-temperature synthesis is the most commonly used method, especially for the stable CPs. In contrast, MTI is most commonly used to synthesize the metastable compounds with ΔH_d > 47 meV/atom. For the subset of CPs synthesized via MTI, the 90th percentile of ΔH_d is 65 meV/atom. This is consistent with failed efforts to synthesize highly metastable CPs at high temperatures (e.g., $HgMo_6Se_8$, ΔH_d = 59 meV/atom),[19] despite successful synthesis via MTI.[47] MTI may therefore enable synthesis of metastable CPs in the range 47 <

https://doi.org/10.1021/jacs.1c02971
J. Am. Chem. Soc. 2021, 143, 9113−9122

ΔH_d < 65 meV/atom that are less likely to be accessible via high-temperature synthesis, enabling a large stability window for the synthesizability of CPs. Above 65 meV/atom, CPs are increasingly less likely to be synthesizable, although the maximum ΔH_d among this set is 83 meV/atom. In order to approximate the probability that H_δ misclassifies CP synthesizability relative to these boundaries, we added noise to the 438 DFT-calculated ΔH_ds using a Gaussian distribution with σ = 32.6 meV/atom (see Experimental Section). With this noise, ∼16% of CPs are misclassified relative to the 65 meV/atom upper boundary for synthesizability, and the false positive rate for CPs predicted to be synthesizable is ∼7%. The probability that a material is misclassified decreases as the difference between the predicted ΔH_d and the upper synthesizability boundary increases.

We generated 205 548 CP compositions and applied H_δ to predict their ΔH_ds (Figure S3). These compositions were generated from up to two chalcogenides and three cations (63 total), with the sum of the cation coefficients limited to ≤2 (see Experimental Section). Although H_δ was developed for single-chalcogenide CPs, it predicts ΔH_d of mixed chalcogenide CPs (e.g., $Mo_6S_4Se_4$) with similar accuracy (mean absolute error, MAE = 26 meV/atom and RMSE = 33 meV/atom on 27 mixed CPs, Figure 4a,b). Mixed chalcogenide CPs are included because they show promise as battery electrodes, electrocatalysts, and thermoelectrics.[13,58,59] Furthermore, our calculations indicate that varying chalcogenide stoichiometry results in linear control over CP band gaps (1.52, 1.48, 1.46, and 1.38 eV for x = 0, 2, 4, and 8 in $Mg_2Mo_6S_{8-x}Se_x$), expanding the potential applications of these phases to photovoltaics and photoelectrocatalysts.

Categorizing these 205 548 CPs using the 90th percentile boundaries for the various reaction temperatures (see above) indicates that 2877 (1.4%) of these compositions are predicted to be stable (ΔH_d < 0 meV/atom); 24 255 (11.8%) are metastable and directly synthesizable via high-temperature methods (0 ≤ ΔH_d < 47 meV/atom); and 21 369 (10.4%) are metastable and synthesizable via MTI (47 ≤ ΔH_d < 65 meV/atom). The remaining 157 047 (76.4%) compositions are predicted to be unstable (ΔH_d ≥ 65 meV/atom) by these definitions.

Synthesis of Chevrel Phase Tellurides. The multinary CP tellurides are an ideal chemical space to validate the accuracy of H_δ for predicting synthesizability and to investigate our predictions of site 2 preference among these phases, which may make them attractive as advanced battery materials and electrocatalysts. Furthermore, the CP telluride space is sparse, with only five synthesized phases ($M_yMo_6Te_8$, M = Cu, Ag, Ni, y = 0.85−2), of which refined atomic coordinates and interatomic separations have only been reported for $Ni_{0.85}Mo_6Te_8$.[23,24] We selected five CP telluride compositions to target for synthesis that have not been previously reported and that H_δ predicts are synthetically accessible (MMo_6Te_8, M = K, Ti, V, Cr, Fe), three of which are calculated to have preferential site 2 occupancy. We also selected one CP telluride that H_δ predicts to be unstable ($Ni_2Mo_6Te_8$). High-temperature direct synthesis was attempted for all of the targeted CPs, and MTI into the binary Mo_6Te_8 was attempted when direct synthesis was unsuccessful (Table 1). DFT-calculated ΔH_ds are included alongside H_δ predictions in Table 1. The MAE between H_δ and DFT on this subset (39.4 meV/atom) is larger than that of the full test set (26.0 meV/atom); however this increased error is not unexpected due to the prevalence of TM intercalants in this subset that are known to be less accurately predicted by SCAN relative to other elements.[30,60] Despite this larger error, H_δ and DFT both accurately categorize all materials relative to the upper synthesizability boundary of 65 meV/atom.

Table 1. Synthesis Results and Computed Stabilities of Seven CP Tellurides[a]

Chevrel composition	H_δ	DFT ΔH_d	synthesis technique
KMo_6Te_8	16.2	36.6	MTI
$FeMo_6Te_8$	45.2	21.4	high temp. direct
$TiMo_6Te_8$	47.2	−2.9	high temp. direct
$CrMo_6Te_8$	50.8	−0.1	high temp. direct
VMo_6Te_8	62.0	−13.6	high temp. direct
$Ni_{1.32}Mo_6Te_8$	62.9	41.1	high temp. direct
$Ni_2Mo_6Te_8$	113.0	79.5	failed

[a]Synthesis of six telluride CPs was attempted, of which five were predicted to be synthesizable. Their compositions are listed alongside their calculated ΔH_d from H_δ and DFT and the synthesis technique used to produce each phase. $Ni_{1.32}Mo_6Te_8$ was not targeted for synthesis but was identified from the failed synthesis of $Ni_2Mo_6Te_8$, which was predicted to not be synthesizable and used as a negative test.

All of the CP tellurides except KMo_6Te_8 and $Ni_2Mo_6Te_8$ were successfully synthesized via microwave-assisted high-temperature reactions of the element precursors. This is the first report of microwave-assisted synthesis of multinary CP tellurides. Synthesis of $Ni_2Mo_6Te_8$ was unsuccessful, which instead yielded $Ni_{1.32}Mo_6Te_8$, a new stoichiometry for Ni-intercalated Mo_6Te_8 (Table 1). This demonstrates the predictive ability of H_δ in conjunction with the established synthetic boundaries, which predict that $Ni_2Mo_6Te_8$ is unstable, whereas a Ni content of 1.32 per Mo_6Te_8 approaches the highest Ni content (1.36) composition within the ΔH_d boundary of 65 meV/atom (Figure S4).

MTI was necessary to synthesize KMo_6Te_8. This is the first report of successful synthesis of a large alkali metal (K, Rb, Cs) intercalated CP with refined atomic coordinates. The attempted high-temperature direct synthesis yielded a mixture of $MoTe_2$ and KMo_3Te_3, a chalcogenide-deficient 1D pseudo-Chevrel phase (Figure S5). The sulfide analogue KMo_3S_3 was previously preferentially synthesized over KMo_6S_8 by high-temperature (∼750 °C) direct synthesis.[61] The structural similarity of these pseudo-CPs likely results in lower kinetic barriers to decomposition into these phases, necessitating the use of MTI to synthesize large alkali metal intercalated CPs (e.g., KMo_6Te_8) despite their predicted and calculated ΔH_ds falling below the MTI range. DFT indicates that KMo_3Te_3 is the stable decomposition product for KMo_6Te_8. Although H_δ correctly classifies the five synthesized CPs with TM intercalants as being synthesizable, four of these materials are classified in the MTI synthesizability range of 47 to 65 meV/atom, indicating the greater challenge of predicting ΔH_d for materials with TM elements. However, DFT still correctly classifies these five materials as being accessible via high-temperature synthesis.

Bulk and surface CP compositions were determined via energy dispersive X-ray spectroscopy (EDX) and X-ray photoelectron spectroscopy (XPS), respectively (Figures S6−S17). Scanning electron microscopy (SEM) and powder X-ray diffraction (PXRD) (Figure 5) indicate that the synthesized CP tellurides are less crystalline than previously reported CP

https://doi.org/10.1021/jacs.1c02971
J. Am. Chem. Soc. 2021, 143, 9113−9122

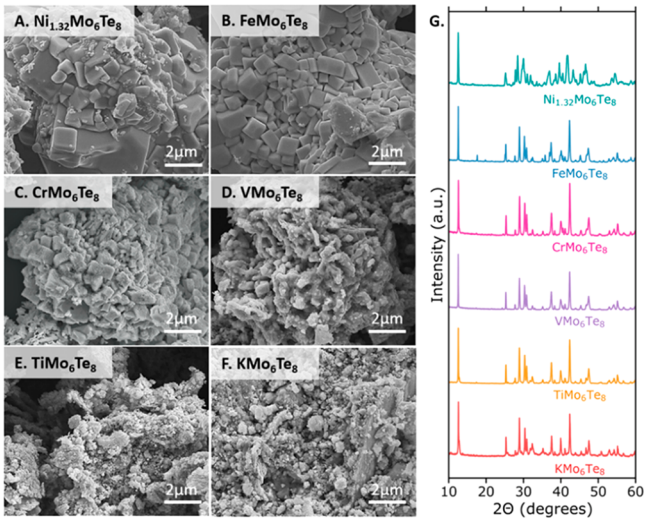

Figure 5. SEM micrographs of intercalated Mo_6Te_8. SEM micrographs of Mo_6Te_8 intercalated with (A) Ni, (B) Fe, (C) Cr, (D) V, (E) Ti, and (F) K depict decreasing crystallinity as cation electropositivity increases. (G) PXRD spectra of the synthesized CP tellurides. Rietveld refinement of the CPs with M = Fe, Cr, V, and Ti indicates that most cations occupy site 2 channels, confirming the predicted preference for this site in our data set.

sulfides and selenides obtained through microwave-assisted synthesis.[13,17,20,25] The crystallinity of this series decreases with increasing cation electropositivity. To confirm the predictions of channel site preference for the TM-intercalated CP tellurides with y = 1 (Figure 3), Rietveld refinement was performed using site 1 off-center and site 2 occupancy (Figures S6ab, S8ab, S10ab, S12ab). For all of the phases, improved refinement results were obtained for site 2 over site 1 off-center. However, both fits have large weighted-profile R-factors (R_{wp}), suggesting a mixture of both phases. This agrees with our data set, which predicts that a mixture of site 1 and site 2 occupancy should be observed, with site 2 being more prevalent at ambient conditions. The poor crystallinity of the CP tellurides yielded low signal-to-noise ratios and large full-profile fitting factors (Tables S5 and S6). Although the crystallinity of these phases may be increased by using slower heating rates, low CP crystallinity may be desirable in applications where high surface area improves performance (e.g., electrocatalysis).

CONCLUSION

The renewed interest in multinary CPs has been driven by recent examples of their promise for advanced energy storage and conversion technologies, including electrocatalysts and battery materials. To overcome the gap between known and possible CP compositions, we developed the interpretable descriptor H_δ to predict CP stability and to enable the rapid identification of synthesizability when applied alongside data-driven boundaries that bracket synthesized materials. H_δ was trained on 438 CPs, which greatly expands upon the current space of computationally characterized CPs and includes properties such as band gap and magnetic moment to guide experiments in key applications. The prediction and experimental verification of site 2 occupancy in CP tellurides in this data set opens a new route for tuning CP properties that may be relevant for battery and electrocatalyst applications, owing to the additional interstitial volume that is now synthetically accessible for intercalant occupation. Furthermore, H_δ was used to predict over 48 000 CPs as synthesizable and their likely synthesis conditions from a set of >200 000 compositions. We anticipate that this set will catalyze exploration of this auspicious material class. More broadly, the SIFT method can be applied to develop accurate and interpretable descriptors for other materials properties, and we expect that our combined computational and experimental approach is transferable to other material classes to accurately predict ΔH_f and ΔH_d, to identify synthesizable materials and to validate their existence.

EXPERIMENTAL SECTION

Data Generation. CP structures were generated stochastically by first selecting the chalcogenide (S, Se, or Te) from a uniform distribution and then selecting the total number of intercalated cations. For compositions with a single cation, the cation was chosen from a set of 53 unique elements (Table S7), and three structures were generated with the cation positioned at (0,0,0), at (0.95, 0.15, 0.9), or at (0, 0.5, 0). These three positions represent site 1, site 1 off-center, and site 2 cation positions. A total of 154 single cation compositions were generated. For compositions with two cations, the first cation was selected from a set of 17 unique elements (Table S7). We set a 10% probability of the second cation being the same element as the first cation to increase the number of ternary CPs in the data set; otherwise, it was selected from a uniform distribution of the remaining 16 cations. Two structures were generated for each double cation composition with the cations positioned at (0.95, 0.15, 0.9) and (0.05, 0.85, 0.1), or (0,0,0) and (0,0.5,0), where the cation with the larger ionic radius was placed at the first of the two positions for each structure. A total of 281 double cation compositions were generated. Ground-state structures for all elemental reference states used in this study were obtained from Materials Project and were further relaxed. All relaxations were performed using the Strongly Constrained and Appropriately Normed (SCAN)[62] density functional and the Vienna Ab initio Simulation Package (VASP).[63] SCAN was selected over the conventional PBE functional for its superior accuracy for calculating ΔH_f and ΔH_d, relative to experiment,[30,60] and for its accuracy for ordering polymorph stability.[64] The errors between SCAN ΔH_d and experiment increase ~45% for materials with transition metals; however these errors are still about 50% lower than those of PBE.[30]

The ion positions and unit cell lattice vectors were allowed to independently optimize during structure relaxation; symmetry constraints were not used. A plane wave cutoff of 520 eV and a Γ-centered Monkhorst–Pack k-point grid with a density of 1200/number-of-atoms were used for all calculations. ΔH_f values were calculated as the difference between the minimized CP total energies (E_{CP}) and the sum of the reference element total energies for each atom in the CP unit cell (eq 2).

$$\Delta H_f = E_{CP} - \sum_{el}^{\text{atoms in unit cell}} E_{ref}(el) \quad (2)$$

$$\Delta H_{d,i} = \Delta H_{f,i} - \text{Min}_{\vec{x}}\left(\sum_{j}^{n} x_j \Delta H_{f,j}|_{i\neq j}\right) \quad (3)$$

ΔH_d were calculated from ΔH_f using the convex hull method (eq 3) where $\vec{x}$ is the array of stoichiometries for all competing phases (n) that minimizes the summation term with the constraints that the atoms in material i must be conserved: $\overrightarrow{\text{atoms}}_i = \sum_j^n x_j^* \overrightarrow{\text{atoms}}_j|_{j\neq i}$ and all $x_j \geq 0$. ΔH_f for competing phases used in the convex hull construction were obtained from ref 30; 211 binary chalcogenides were included in this set (Table S8). This data set did not include competing phases for the chalcogenides of Be, Sc, V, Co, Rb, Nb, La, Ce, Pr, Nd, Sm, Tb, Dy, Hf, Ta, Os, Re, and Ir. For this set of elements, the structures of the stable chalcogenide (S, Se, Te) binary

https://doi.org/10.1021/jacs.1c02971
J. Am. Chem. Soc. 2021, 143, 9113−9122

phases were obtained from Materials Project and relaxed using the aforementioned calculation standards. A total of 154 of these structures were obtained and relaxed to be used as additional competing phases (Table S9). Furthermore, we generated and relaxed a set of nine 1D pseudo-CPs for the cations Na, K, and Rb and the chalcogenides S, Se, and Te, as these have been previously demonstrated as competing phases for CPs with these cations.[61]

Boltzmann factors were calculated using eq 4, where $\Delta H_{d,i}$ is the decomposition enthalpy of cation site configuration i, $\Delta H_{d,min}$ is the minimum ΔH_d of the CP composition, and k_b is Boltzmann's constant.

$$p_i = \exp((\Delta H_{d,i} - \Delta H_{d,min})/k_b T) \quad (4)$$

The set of 205 548 CP compositions was generated from 63 cations, 53 of which are included in Table S7 and the remaining 10 are As, W, Pm, Eu, Gd, Ho, Er, Tm, Yb, and Lu. Up to three cations were allowed per generated composition, with the sum of the coefficients limited to ≤2 and the coefficients being within the set: 0, 0.5, 1, 1.5, 2. The sum of cation coefficients was limited to ≤1 for compositions containing cations with average ionic radii greater than that of Mg, which is the largest cation with coefficients greater than 1 in the experimental CP set. The limits on cation stoichiometry were chosen to reduce the degree of extrapolation beyond the training and testing sets, where the accuracy of H_δ is not quantified. Allowed chalcogenides and mixed chalcogenide coefficients are S_8, S_6Se_2, S_4Se_4, S_2Se_6, Se_8, Se_6Te_2, Se_4Te_4, Se_2Te_6, Te_8, S_6Te_2, S_4Te_4, and S_2Te_6.

Machine Learning. Symbolic regression methods involve recursively combining features (e.g., electronegativity) via mathematical operations (e.g., +, −, *) to develop increasingly complex functions that describe a target property (e.g., ΔH_d), and methods such as SISSO and GPlearn have been used to develop impressive materials science models.[35,36,65,66] However, given a large set of mathematical operations or primary features, the set of generated features in each iteration can quickly become computationally intractable. To address this, we developed the SIFT machine learning method.

A block flow diagram for SIFT is shown in Figure S1. SIFT was implemented in Python 3 and is available at 10.5281/zenodo.4796358. Inputs to SIFT include a matrix of data where the rows are unique entries (i.e., materials) and the columns are primary features (e.g., pol_M, pol_X), a vector containing the target property for each unique entry in the same order as the data matrix, the number of iterations of combining features, and the number of features retained after each iteration. Optionally, a python dictionary containing each primary feature and its respective units can be input to SIFT. This allows the user to limit how features can be combined based on their units; addition, subtraction, and division will operate only between features with the same units, and multiplication will be performed only if at least one of the two features is unitless to limit unit complexity. Depending on the application, these restrictions can be modified to allow for potentially more complex models. For this work, we restricted feature combinations based on units and only used the mathematical operations addition, subtraction, division, and multiplication. A total of 62 primary features were used for SIFT to develop H_δ (Table S10).

SIFT begins by generating all of the allowed feature combinations (limited based on defined unit and maximum complexity constraints) from the primary feature set and calculating the RMSE between the generated feature combinations and the target property. The generated features are then ranked by their RMSE, and this set is trimmed to only retain the lowest error generated features using a predefined cutoff. These are then combined with the primary feature set for the current iteration to be used as the starting feature set for the following iteration. In this work we retained the 500 best generated features after each iteration. SIFT is similar to the SISSO approach,[35] which also iteratively combines a set of primary features to develop an increasingly large set of feature combinations. However, the intermediate feature trimming step in SIFT significantly improves scaling over multiple iterations and allows for a larger set of primary features, at the expense of being less comprehensive by not retaining all generated features at each step as SISSO does. We ran SIFT for three iterations in this work to develop a sufficiently accurate model. The maximum complexity allowed for the SIFT models was set to six total features (e.g., $(A/B - C) + D/E + A$). H_δ and SIFT, using the specified parameters, were benchmarked against other ML methods in Section S1, including SIFT with different parameters that enabled greater model complexity. Eighty percent of the compositions in our data set were used for training SIFT, and the remainder were used for testing; only the most stable cation configuration for each of the 438 compositions was used for model development.

Fifty-five of the 62 initial features used in this work to describe CP compositions were derived from 21 elemental properties obtained from Matminer and WebElements (see Table S10).[67] This data set of elemental properties was initially compiled for use in refs 36 and 65. Five of the 62 initial features were derived from oxidation states that were calculated for each CP composition using the 'add_charges_from_oxi_state_guesses' function in Pymatgen.[68] Oxidation states were fixed to −2 for the three chalcogenides and were constrained to be either +1, +2, or +3 for the Mo atoms. Cation oxidation states were constrained to be greater than zero. The electrons donated from the cation, e_d in H_δ, are calculated as the sum of the oxidation states of the intercalated cations and are limited to $0 \le e_d \le 4$. The remaining two initial features were calculated directly from the composition (i.e., the total number of elements and the number of intercalated cations). Features were normalized by dividing by a normalization constant. For average features of M and features of X, the normalization constant was the largest magnitude value (i.e., the max or min) of the respective feature (f) resulting in a feature range of $-1 \le f \le 1$. For total features of M (i.e., the sum of the feature over all cations in the composition) the normalization constant was halved, resulting in a feature range of $-2 \le f \le 2$ so that cation stoichiometry was considered in feature magnitude.

H_δ directly predicts ΔH_d (i.e., $H_\delta = \Delta H_d$). As a result, CP ΔH_f values can also be calculated from H_δ using eq 5, which is derived from eq 3.

$$\Delta H_{f,i} = H_{\delta,i} + \mathrm{Min}_{\vec{x}}\left(\sum_j^n x_j \Delta H_{f,j}|_{i\neq j}\right) \quad (5)$$

We approximated the probability that H_δ (or a model with equivalent accuracy) will correctly classify CP synthesizability with respect to the MTI upper synthesizability boundary (i.e., 65 meV/atom) by adding noise to the ΔH_d values of the 438 CPs in our data set. Noise was applied using a Gaussian distribution centered at each ΔH_d with a standard deviation (σ) equivalent to the RMSE of H_δ on the test set (32.6 meV/atom). With this added noise, we calculated the percent of CPs that were still classified correctly as synthesizable or not synthesizable (i.e., < or >65 meV/atom). The false positive rate was obtained from the subset of incorrectly classified CPs where the noisy ΔH_d indicated that the CP was synthesizable (<65 meV/atom), but the calculated ΔH_d indicated that the CP was not synthesizable (>65 meV/atom). Classification percentages were averaged over 100 runs.

Chemicals and Materials. Cr (99.95%, ∼200 mesh), V (99.5%, ∼325 mesh), Ti (99.5%, ∼325 mesh), and Fe (99.998%, ∼200 mesh) powders, and K (99.95%) metal were used as purchased from Alfa Aesar. Mo powder (99.99%, ∼100 mesh) and Te powder (99.8%, ∼200 mesh) were used as purchased from Sigma-Aldrich. Al_2O_3 microfiber was used as purchased from ThermoFisher. Fused quartz tubes (2 mm thick) were purchased from AdValue Technology and made into round-bottom tubes with an in-house oxy-hydrogen torch.

Telluride Synthesis. The CPs studied herein were synthesized through a previously described microwave-assisted solid-state synthesis approach.[17,20] The general procedure involved weighing stoichiometric amounts of the appropriate precursors in a dry N_2 glovebox, followed by ball-milling and hydraulic pressing to attain a homogenized pellet. The pellets were transferred into quartz tubes and packed under N_2 with Al_2O_3 microfiber. The tubes were placed

https://doi.org/10.1021/jacs.1c02971
J. Am. Chem. Soc. 2021, 143, 9113−9122

inside an alumina crucible filled with fine-mesh graphite powder. This reaction vessel was placed inside a conventional microwave oven under an Ar atmosphere. Samples were irradiated for 10 min at a power of up to 1000 W. The color temperatures of the graphite powder and the quartz tube were monitored to maintain the temperature between 900 and 1000 °C for Mo_6Te_8 and $M_yMo_6Te_8$ (M = Ti, V, Cr, Fe, Ni). Impurities such as $MoTe_2$ and Mo were observed if synthesis temperatures were below 900 °C or above 1000 °C, respectively. KMo_6Te_8 was obtained through MTI by similarly mixing and pressing the metallic potassium with Mo_6Te_8 and maintaining the microwave temperature at just below 450 °C for 10 min. Decomposition of Mo_6Te_8 at higher temperatures was observed.

Structural Characterization. The phase purity of each CP was analyzed via PXRD using a Bruker D8 Advance diffractometer with Cu K-alpha radiation (1.5406 Å). Catalyst morphology and bulk composition were analyzed using a FEI (Hillsboro, OR, USA) 430 Nano SEM and a FEI Scios dual-beam SEM with an Oxford EDX detector, respectively. Composition stoichiometry was confirmed by averaging the EDX average atomic % over multiple sites, which agree with an MMo_6Te_8 composition for M = K, Ti, V, Cr, and Fe within an ~1% error based on instrumental counting statistics. Surface composition analysis was performed using a PHI Versaprobe 3 XPS for all synthesized CPs aside from VMo_6Te_8, which was analyzed using a Kratos Supra Axis XPS. Rietveld refinements were performed with Topas diffraction analysis software from Bruker.

Data sets and code are available for free at 10.5281/zenodo.4796358.

■ ASSOCIATED CONTENT

Supporting Information

The Supporting Information is available free of charge at https://pubs.acs.org/doi/10.1021/jacs.1c02971.

> Additional details, figures, and tables including the H_δ benchmarking, a block flow diagram of SIFT, ΔH_d of 67 known CPs, distribution of ΔH_d for predicted CPs, PXRD, EDX, and XPS spectra, magnetic and conductive phase-change CPs, elemental values of H_δ parameters, synthesis conditions of 67 known CPs, lattice parameters of synthesized tellurides, the set of cations used for data set generation, competing phases for ΔH_d calculations, and the set of 62 primary features used to run SIFT (PDF)

Accession Codes

CCDC 2071028−2071036 contain the supplementary crystallographic data for this paper. These data can be obtained free of charge via www.ccdc.cam.ac.uk/data_request/cif, or by emailing data_request@ccdc.cam.ac.uk, or by contacting The Cambridge Crystallographic Data Centre, 12 Union Road, Cambridge CB2 1EZ, UK; fax: +44 1223 336033.

■ AUTHOR INFORMATION

Corresponding Authors

Jesús M. Velázquez − *Department of Chemistry, University of California Davis, Davis, California 95616, United States;* orcid.org/0000-0003-2790-0976; Email: jevelazquez@ucdavis.edu

Charles B. Musgrave − *Department of Chemical and Biological Engineering, Materials Science and Engineering Program, and Renewable and Sustainable Energy Institute, University of Colorado Boulder, Boulder, Colorado 80303, United States;* orcid.org/0000-0002-5732-3180; Email: charles.musgrave@colorado.edu

Authors

Nicholas R. Singstock − *Department of Chemical and Biological Engineering, University of Colorado Boulder, Boulder, Colorado 80303, United States;* orcid.org/0000-0003-2093-0216

Jessica C. Ortiz-Rodríguez − *Department of Chemistry, University of California Davis, Davis, California 95616, United States*

Joseph T. Perryman − *Department of Chemistry, University of California Davis, Davis, California 95616, United States*

Christopher Sutton − *Department of Chemistry and Biochemistry, University of South Carolina, Columbia, South Carolina 29208, United States*

Complete contact information is available at: https://pubs.acs.org/10.1021/jacs.1c02971

Notes

The authors declare no competing financial interest.

■ ACKNOWLEDGMENTS

N.R.S. was supported by the National Science Foundation (CBET-2016225) and by a U.S. Department of Education Graduate Assistance in Areas of National Need Fellowship under the Materials for Energy Conversion and Sustainability program. J.O.R. was funded by the National Science Foundation Graduate Research Fellowship (NSF 1650042). J.M.V. thanks the University of California, Davis, for start-up funding, as well as support from the Cottrell Scholar program supported by the Research Corporation for Science Advancement (RCSA 26780). J.M.V. also acknowledges funding support from the NSF through the Faculty Early Career Development Program (DMR-2044403). Part of this work was performed at the Stanford Nano Shared Facilities (SNSF)/Stanford Nanofabrication Facility (SNF), supported by the National Science Foundation under award ECCS-1542152. XPS analysis at UC Davis was supported by the National Science Foundation (DMR-1828238). A portion of the research was performed using computational resources sponsored by the Department of Energy's Office of Energy Efficiency and Renewable Energy and located at the National Renewable Energy Laboratory.

■ REFERENCES

(1) Matthias, B. T.; Marezio, M.; Corenzwit, E.; Cooper, A. S.; Barz, H. E. High-Temperature Superconductors, the First Ternary System. *Science (Washington, DC, U. S.)* **1972**, *175* (4029), 1465−1466.

(2) Peña, O. Chevrel Phases: Past, Present and Future. *Phys. C* **2015**, *514*, 95−112.

(3) Xue, W.; Shi, Z.; Suo, L.; Wang, C.; Wang, Z.; Wang, H.; So, K. P.; Maurano, A.; Yu, D.; Chen, Y.; et al. Intercalation-Conversion Hybrid Cathodes Enabling Li-S Full-Cell Architectures with Jointly Superior Gravimetric and Volumetric Energy Densities. *Nat. Energy* **2019**, *4* (5), 374−382.

(4) Suo, L.; Borodin, O.; Gao, T.; Olguin, M.; Ho, J.; Fan, X.; Luo, C.; Wang, C.; Xu, K. "Water-in-Salt" Electrolyte Enables High-Voltage Aqueous Lithium-Ion Chemistries. *Science (Washington, DC, U. S.)* **2015**, *350* (6263), 938−943.

(5) Choi, J. W.; Aurbach, D. Promise and Reality of Post-Lithium-Ion Batteries with High Energy Densities. *Nat. Rev. Mater.* **2016**, *1*, 16013 DOI: 10.1038/natrevmats.2016.13.

(6) Liang, Y.; Dong, H.; Aurbach, D.; Yao, Y. Current Status and Future Directions of Multivalent Metal-Ion Batteries. *Nature Energy* **2020**, *5*, 646-656 DOI: 10.1038/s41560-020-0655.

(7) Wang, F.; Lin, Y.; Suo, L.; Fan, X.; Gao, T.; Yang, C.; Han, F.; Qi, Y.; Xu, K.; Wang, C. Stabilizing High Voltage LiCoO2 Cathode in Aqueous Electrolyte with Interphase-Forming Additive. *Energy Environ. Sci.* **2016**, *9* (12), 3666−3673.
(8) Aurbach, D.; Lu, Z.; Schechter, A.; Gofer, Y.; Gizbar, H.; Turgeman, R.; Cohen, Y.; Moshkovich, M.; Levi, E. Prototype Systems for Rechargeable Magnesium Batteries. *Nature* **2000**, *407* (6805), 724−727.
(9) Malchik, F.; Shpigel, N.; Levi, M. D.; Mathis, T. S.; Mor, A.; Gogotsi, Y.; Aurbach, D. Superfast High-Energy Storage Hybrid Device Composed of MXene and Chevrel-Phase Electrodes Operated in Saturated LiCl Electrolyte Solution. *J. Mater. Chem. A* **2019**, *7* (34), 19761−19773.
(10) Lu, K.; Gao, S.; Li, G.; Kaelin, J.; Zhang, Z.; Cheng, Y. Regulating Interfacial Na-Ion Flux via Artificial Layers with Fast Ionic Conductivity for Stable and High-Rate Na Metal Batteries. *ACS Mater. Lett.* **2019**, *1* (3), 303−309.
(11) Lu, K.; Gao, S.; Dick, R. J.; Sattar, Z.; Cheng, Y. A Fast and Stable Li Metal Anode Incorporating an Mo6S8 Artificial Interphase with Super Li-Ion Conductivity. *J. Mater. Chem. A* **2019**, *7* (11), 6038−6044.
(12) Agiorgousis, M. L.; Sun, Y. Y.; West, D.; Zhang, S. Intercalated Chevrel Phase Mo6S8 as a Janus Material for Energy Generation and Storage. *ACS Appl. Energy Mater.* **2018**, *1* (2), 440−446.
(13) Ortiz-Rodríguez, J. C.; Singstock, N. R.; Perryman, J. T.; Hyler, F. P.; Jones, S. J.; Holder, A. M.; Musgrave, C. B.; Velázquez, J. M. Stabilizing Hydrogen Adsorption through Theory-Guided Chalcogen Substitution in Chevrel-Phase Mo6X8 (X = S, Se, Te) Electrocatalysts. *ACS Appl. Mater. Interfaces* **2020**, *12* (32), 35995−36003.
(14) Naik, K. M.; Sampath, S. Cubic Mo6S8-Efficient Electrocatalyst Towards Hydrogen Evolution Over Wide PH Range. *Electrochim. Acta* **2017**, *252*, 408−415.
(15) Jiang, J.; Gao, M.; Sheng, W.; Yan, Y. Hollow Chevrel-Phase NiMo3S4 for Hydrogen Evolution in Alkaline Electrolytes. *Angew. Chem., Int. Ed.* **2016**, *55* (49), 15240−15245.
(16) Fischer, C.; Alonso-Vante, N.; Fiechter, S.; Tributsch, H. Electrocatalytic Properties of Mixed Transition Metal Tellurides (Chevrel-Phases) for Oxygen Reduction. *J. Appl. Electrochem.* **1995**, *25* (11), 1004−1008.
(17) Perryman, J. T.; Ortiz-Rodríguez, J. C.; Jude, J. W.; Hyler, F. P.; Davis, R. C.; Mehta, A.; Kulkarni, A. R.; Patridge, C. J.; Velázquez, J. M. Metal-Promoted Mo6S8 Clusters: A Platform for Probing Ensemble Effects on the Electrochemical Conversion of CO2 and CO to Methanol. *Mater. Horiz.* **2020**, *7*, 193-202.
(18) Liu, C.; Liu, P. Mechanistic Study of Methanol Synthesis from CO2 and H2 on a Modified Model Mo6S8 Cluster. *ACS Catal.* **2015**, *5* (2), 1004−1012.
(19) Umarji, A. M.; Rao, G. V. S.; Janawadkar, M. P.; Radhakrishnan, T. S. Metal Atom Incorporation Studies on AxMo6S8 Chevrel Phases. *J. Phys. Chem. Solids* **1980**, *41* (5), 421−429.
(20) Perryman, J. T.; Hyler, F. P.; Ortiz-Rodríguez, J. C.; Mehta, A.; Kulkarni, A. R.; Velázquez, J. M. X-Ray Absorption Spectroscopy Study of the Electronic Structure and Local Coordination of 1st Row Transition Metal-Promoted Chevrel-Phase Sulfides. *J. Coord. Chem.* **2019**, *72* (8), 1322−1335.
(21) Mei, L.; Xu, J.; Wei, Z.; Liu, H.; Li, Y.; Ma, J.; Dou, S. Chevrel Phase Mo6T8 (T = S, Se) as Electrodes for Advanced Energy Storage. *Small* **2017**, *13* (34), 1701441.
(22) Levi, E.; Gershinsky, G.; Aurbach, D.; Isnard, O.; Ceder, G. New Insight on the Unusually High Ionic Mobility in Chevrel Phases. *Chem. Mater.* **2009**, *21* (7), 1390−1399.
(23) Honle, W.; Yvon, K. Einkristalluntersuchung an Ni0.8Mo6Te8 Mit Triklin Verzerrten Mo6-Oktaedern. *Int. J. Struct. Phys. Chem. Asp. Cryst. Mater.* **1979**, *162* (1), 103−104.
(24) Shi, X.; Wang, L.; Chen, L.; Chen, X. Thermoelectric Properties of MxMo6Te8 (M = Ag, Cu). *Trans. Nonferrous Met. Soc. China* **2009**, *19* (3), 642−645.
(25) Lilova, K.; Perryman, J. T.; Singstock, N. R.; Abramchuk, M.; Subramani, T.; Lam, A.; Yoo, R.; Ortiz-Rodríguez, J. C.; Musgrave, C. B.; Navrotsky, A.; Velázquez, J. M. A Synergistic Approach to Unraveling the Thermodynamic Stability of Binary and Ternary Chevrel Phase Sulfides. *Chem. Mater.* **2020**, *32*, 7044−7051.
(26) Ward, L.; Agrawal, A.; Choudhary, A.; Wolverton, C. A General-Purpose Machine Learning Framework for Predicting Properties of Inorganic Materials. *npj Comput. Mater.* **2016**, *2* (1), 1−7.
(27) Jha, D.; Ward, L.; Paul, A.; Liao, W.-K.; Choudhary, A.; Wolverton, C.; Agrawal, A. ElemNet: Deep Learning the Chemistry of Materials From Only Elemental Composition. *Sci. Rep.* **2018**, *8*, 17593, DOI: 10.1038/s41598-018-35934-y.
(28) Xie, T.; Grossman, J. C. Crystal Graph Convolutional Neural Networks for an Accurate and Interpretable Prediction of Material Properties. *Phys. Rev. Lett.* **2018**, *120* (14), 145301.
(29) Faber, F. A.; Lindmaa, A.; Von Lilienfeld, O. A.; Armiento, R. Machine Learning Energies of 2 Million Elpasolite (ABC2D6) Crystals. *Phys. Rev. Lett.* **2016**, *117* (13), 135502.
(30) Bartel, C. J.; Weimer, A. W.; Lany, S.; Musgrave, C. B.; Holder, A. M. The Role of Decomposition Reactions in Assessing First-Principles Predictions of Solid Stability. *npj Comput. Mater.* **2019**, *5* (1), 4.
(31) Levi, E.; Aurbach, D. Chevrel Phases, MxMo6T8 (M = Metals, T = S, Se, Te) as a Structural Chameleon: Changes in the Rhombohedral Framework and Triclinic Distortion. *Chem. Mater.* **2010**, *22* (12), 3678−3692.
(32) Levi, E.; Gershinsky, G.; Aurbach, D.; Isnarcr, O. Crystallography of Chevrel Phases, MMo6T8 (M = Cd, Na, Mn, and Zn, T = S, Se) and Their Cation Mobility. *Inorg. Chem.* **2009**, *48* (18), 8751−8758.
(33) Roche, C.; Chevrel, R.; Jenny, A.; Pecheur, P.; Scherrer, H.; Scherrer, S. Crystallography and Density of States Calculation of MxMo6Se8 (M = Ti,Cr,Fe,Ni). *Phys. Rev. B: Condens. Matter Mater. Phys.* **1999**, *60* (24), 16442−16447.
(34) Mançour-Billah, A.; Chevrel, R. A New Increasing Delocalization of M = 3d-Elements (Ti, Fe, Co) in the Channels Network of the Ternary MyMo6Se8 Chevrel Phases. *J. Solid State Chem.* **2003**, *170* (2), 281−288.
(35) Ouyang, R.; Curtarolo, S.; Ahmetcik, E.; Scheffler, M.; Ghiringhelli, L. M. SISSO: A Compressed-Sensing Method for Identifying the Best Low-Dimensional Descriptor in an Immensity of Offered Candidates. *Phys. Rev. Mater.* **2018**, *2* (8), 083802.
(36) Bartel, C. J.; Sutton, C.; Goldsmith, B. R.; Ouyang, R.; Musgrave, C. B.; Ghiringhelli, L. M.; Scheffler, M. New Tolerance Factor to Predict the Stability of Perovskite Oxides and Halides. *Sci. Adv.* **2019**, *5*, No. 2, eaav0693.
(37) Walsh, A.; Sokol, A.; Buckeridge, J.; Scanlon, D.; Catlow, R. Oxidation States and Ionicity. *Nat. Mater.* **2018**, *17*, 958−964.
(38) Sun, W.; Bartel, C. J.; Arca, E.; Bauers, S. R.; Matthews, B.; Orvañanos, B.; Chen, B. R.; Toney, M. F.; Schelhas, L. T.; Tumas, W.; et al. A Map of the Inorganic Ternary Metal Nitrides. *Nat. Mater.* **2019**, *18* (7), 732−739.
(39) Etourneau, J.; Portier, J.; Ménil, F. The Role of the Inductive Effect in Solid State Chemistry: How the Chemist Can Use It to Modify Both the Structural and the Physical Properties of the Materials. *J. Alloys Compd.* **1992**, *188* (C), 1−7.
(40) Kubel, F.; Yvon, K. Structural Phase Transitions in Chevrel Phases Containing Divalent Metal Cations. I. Structure Refinement of Rhombohedral MMo6S8 (M = Eu, Sr, Ba) at Room Temperature. *Acta Crystallogr., Sect. C: Cryst. Struct. Commun.* **1987**, *43* (9), 1655−1659.
(41) Chevreau, N.; Johnson, D. C. Preparation and Physical Properties of BiMo6S8 and SbMo6S8. *J. Solid State Chem.* **1986**, *61* (3), 347−353.
(42) Lachal, B.; Baillif, R.; Junod, A.; Muller, J. Structural Instabilities of Chevrel Phases: The Alkaline Earth Molybdenum Sulphide Series. *Solid State Commun.* **1983**, *45* (9), 849−851.

https://doi.org/10.1021/jacs.1c02971
J. Am. Chem. Soc. 2021, 143, 9113−9122

(43) Fischer, Ø.; Treyvaud, A.; Chevrel, R.; Sergent, M. Superconductivity in the RexMo6S8. *Solid State Commun.* **1975**, *17* (6), 721−724.
(44) Shelton, R. N.; McCallum, R. W.; Adrian, H. Superconductivity in Rare Earth Molybdenum Selenides. *Phys. Lett. A* **1976**, *56* (3), 213−214.
(45) McCarty, K. F.; Anderegg, J. W.; Schrader, G. L. Hydrodesulfurization Catalysis by Chevrel Phase Compounds. *J. Catal.* **1985**, *93* (2), 375−387.
(46) Sergent, M.; Chevrel, R. Sur de Nouvelles Phases Séléniées Ternaires Du Molybdène. *J. Solid State Chem.* **1973**, *6* (3), 433−437.
(47) Tarascon, J. M.; Di Salvo, F. J.; Waszczak, J. V.; Hull, G. W. Synthesis and Peculiar Properties of InMo6S8-xSex, TlMo6S8-xSex, and HgyMo6S8-xSex. *Phys. Rev. B: Condens. Matter Mater. Phys.* **1985**, *31* (2), 1012−1021.
(48) Hohlfeld, C.; Pietrass, B. Determination of the Energy Gap of Superconducting Chevrel and A15 Compounds from Heat Capacity Measurements. *J. Low Temp. Phys.* **1982**, *48* (5−6), 503−513.
(49) Potel, M.; Chevrel, R.; Sergent, M.; Decroux, M.; Fischer, Ø. Nouveaux Clusters Dans Les Chalcogenures Ternaires Derivant Du Molybdene (II). *C. R. Acad. Sci.* **1979**, *288*, 429−432.
(50) Levi, E.; Lancry, E.; Mitelman, A.; Aurbach, D.; Ceder, G.; Morgan, D.; Isnard, O. Phase Diagram of Mg Insertion into Chevrel Phases, MgxMo6T8 (T = S, Se). 1. Crystal Structure of the Sulfides. *Chem. Mater.* **2006**, *18* (23), 5492−5503.
(51) Levi, E.; Mitelman, A.; Isnard, O.; Brunelli, M.; Aurbach, D. Phase Diagram of Mg Insertion into Chevrel Phases, MgxMo6T8 (T = S, Se). 3. The Crystal Structure of Triclinic Mg2Mo6Se8. *Inorg. Chem.* **2008**, *47* (6), 1975−1983.
(52) Levi, E.; Lancry, E.; Mitelman, A.; Aurbach, D.; Isnard, O.; Djurado, D. Phase Diagram of Mg Insertion into Chevrel Phases, MgxMo6T8 (T = S, Se). 2. The Crystal Structure of Triclinic MgMo6Se8. *Chem. Mater.* **2006**, *18* (16), 3705−3714.
(53) Jorgensen, J. D.; Hinks, D. G.; Felcher, G. P. Lattice Instability and Superconductivity in the Pb, Sn, and Ba Chevrel Phases. *Phys. Rev. B: Condens. Matter Mater. Phys.* **1987**, *35* (10), 5365−5368.
(54) Tarascon, J. M.; Orlando, T. P.; Neal, M. J. Rechargeable Lithium Batteries Based on the Ternary Chevrel Phase AgMo6S8 as the Cathode. *J. Electrochem. Soc.* **1988**, *135* (4), 804−808.
(55) Johnson, D. C.; McLean, R. S.; McKinnon, W. R. Structural and Electronic Instabilities in AgMo6Se8. *J. Solid State Chem.* **1989**, *82* (1), 35−42.
(56) Geng, L.; Lv, G.; Xing, X.; Guo, J. Reversible Electrochemical Intercalation of Aluminum in Mo6S8. *Chem. Mater.* **2015**, *27* (14), 4926−4929.
(57) Sun, W.; Dacek, S. T.; Ong, S. P.; Hautier, G.; Jain, A.; Richards, W. D.; Gamst, A. C.; Persson, K. A.; Ceder, G. The Thermodynamic Scale of Inorganic Crystalline Metastability. *Sci. Adv.* **2016**, *2* (11), No. 11, e1600225.
(58) Suresh, G. S.; Levi, M. D.; Aurbach, D. Effect of Chalcogen Substitution in Mixed Mo6S8-nSen (n = 0, 1, 2) Chevrel Phases on the Thermodynamics and Kinetics of Reversible Mg Ions Insertion. *Electrochim. Acta* **2008**, *53* (11), 3889−3896.
(59) Kurosaki, K.; Kosuga, A.; Yamanaka, S. Thermoelectric Properties of Chevrel Phase Mo6Te8-xSx. *J. Alloys Compd.* **2003**, *351* (1−2), 208−211.
(60) Isaacs, E. B.; Wolverton, C. Performance of the Strongly Constrained and Appropriately Normed Density Functional for Solid-State Materials. *Phys. Rev. Mater.* **2018**, *2* (6), 063801.
(61) Perryman, J. T.; Kulkarni, A. R.; Velázquez, J. M. Direct Solid-State Nucleation and Charge-Transport Dynamics of Alkali Metal-Intercalated M2Mo6S6 (M = K, Rb, Cs) Nanorods. *J. Mater. Chem. C* **2020**, *8* (31), 10742−10748.
(62) Sun, J.; Ruzsinszky, A.; Perdew, J. Strongly Constrained and Appropriately Normed Semilocal Density Functional. *Phys. Rev. Lett.* **2015**, *115* (3), 036402, DOI: 10.1103/PhysRevLett.115.036402.
(63) Kresse, G.; Furthmüller, J. Efficient Iterative Schemes for Ab Initio Total-Energy Calculations Using a Plane-Wave Basis Set. *Phys. Rev. B: Condens. Matter Mater. Phys.* **1996**, *54* (16), 11169−11186.
(64) Zhang, Y.; Kitchaev, D. A.; Yang, J.; Chen, T.; Dacek, S. T.; Sarmiento-Pérez, R. A.; Marques, M. A. L.; Peng, H.; Ceder, G.; Perdew, J. P.; et al. Efficient First-Principles Prediction of Solid Stability: Towards Chemical Accuracy. *npj Comput. Mater.* **2018**, *4* (1), 1−6.
(65) Bartel, C. J.; Millican, S. L.; Deml, A. M.; Rumptz, J. R.; Tumas, W.; Weimer, A. W.; Lany, S.; Stevanović, V.; Musgrave, C. B.; Holder, A. M. Physical Descriptor for the Gibbs Energy of Inorganic Crystalline Solids and Temperature-Dependent Materials Chemistry. *Nat. Commun.* **2018**, *9* (1), 4168.
(66) Weng, B.; Song, Z.; Zhu, R.; Yan, Q.; Sun, Q.; Grice, C. G.; Yan, Y.; Yin, W. J. Simple Descriptor Derived from Symbolic Regression Accelerating the Discovery of New Perovskite Catalysts. *Nat. Commun.* **2020**, *11* (1), 3513.
(67) Ward, L.; Dunn, A.; Faghaninia, A.; Zimmermann, N.; Bajaj, S.; Wang, Q.; Montoya, J.; Chen, J.; Bystrom, K.; Dylla, M.; et al. Matminer: An Open Source Toolkit for Materials Data Mining. *Comput. Mater. Sci.* **2018**, *152*, 60−69.
(68) Ong, S. P.; Richards, W. D.; Jain, A.; Hautier, G.; Kocher, M.; Cholia, S.; Gunter, D.; Chevrier, V. L.; Persson, K. A.; Ceder, G. Python Materials Genomics (Pymatgen): A Robust, Open-Source Python Library for Materials Analysis. *Comput. Mater. Sci.* **2013**, *68*, 314−319.

https://doi.org/10.1021/jacs.1c02971
J. Am. Chem. Soc. 2021, 143, 9113−9122